

Strong constraints from COSINE-100 on the DAMA dark matter results using the same sodium iodide target

¹*Department of Physics, University of California San Diego, La Jolla, CA 92093, USA*

²*Department of Physics and Wright Laboratory, Yale University, New Haven, CT 06520, USA*

³*Physics Institute, University of São Paulo, 05508-090, São Paulo, Brazil*

⁴*Department of Physics and Astronomy, Seoul National University, Seoul 08826, Republic of Korea*

⁵*Department of Physics, Bandung Institute of Technology, Bandung 40132, Indonesia*

⁶*Department of Physics and Astronomy, University of Sheffield, Sheffield S3 7RH, United Kingdom*

⁷*Department of Physics, Chung-Ang University, Seoul 06973, Republic of Korea*

⁸*Department of Science Education, Ewha Womans University, Seoul 03760, Republic of Korea*

⁹*Center for Exotic Nuclear Studies, Institute for Basic Science (IBS), Daejeon 34126, Republic of Korea*

¹⁰*IBS School, University of Science and Technology (UST), Daejeon 34113, Republic of Korea*

¹¹*Center for Underground Physics, Institute for Basic Science (IBS), Daejeon 34126, Republic of Korea*

¹²*Department of Physics and Wisconsin IceCube Particle Astrophysics Center,*

University of Wisconsin-Madison, Madison, WI 53706, USA

¹³*Department of Physics, Kyungpook National University, Daegu 41566, Republic of Korea*

¹⁴*Department of Physics, Sejong University, Seoul 05006, Republic of Korea*

¹⁵*Korea Research Institute of Standards and Science, Daejeon 34113, Republic of Korea*

¹⁶*Department of Accelerator Science, Korea University, Sejong 30019, Republic of Korea*

¹⁷*Department of Physics, Sungkyunkwan University, Suwon 16419, Republic of Korea*

(Dated: August 27, 2021)

We present new constraints on dark matter interactions using 1.7 years of COSINE-100 data. The COSINE-100 experiment, consisting of 106 kg of thallium-doped sodium iodide (NaI(Tl)) target material, is aimed at testing DAMA's claim of dark matter observation using the same NaI(Tl) detectors. Improved event selection requirements, a more precise understanding of the detector background and the use of a larger data set considerably enhances the COSINE-100 sensitivity for dark matter detection. No signal consistent with the dark matter interaction is identified, and rules out model-dependent dark matter interpretations of the DAMA signals in the specific context of standard halo model with the same NaI(Tl) target for various interaction hypotheses.

* yjko@ibs.re.kr

† hyunsulee@ibs.re.kr

consistency between DAMA and COSINE-100. Model independent searches of an annual modulation signal using 1.7 years data were also reported but were still not sensitive enough to conclusively challenge the DAMA observation [22]. Here we present results from an analysis of 1.7 years of COSINE-100 data with improved event selection requirements and an energy threshold that has been reduced from 2 keVee to 1 keVee, where keVee is kiloelectron volt electron-equivalent energy [27]. We find an order of magnitude improvement in sensitivity, sufficient for the first time to strongly constrain these alternative scenarios, as well as to further strengthen the previously observed inconsistency with the WIMP-nucleon spin-independent interaction hypothesis [21].

RESULTS

Experiment

COSINE-100 is located at the Yangyang Underground Laboratory in South Korea with a 700 m rock overburden [21, 22]. The experiment consists of eight low-background thallium-doped sodium iodide (NaI(Tl)) crystals arranged in a 4×2 array with a total target mass of 106 kg. The array is immersed in 2,200 L of liquid scintillator used to identify events induced by radioactive background sources that are inside or outside the crystals [28]. The liquid scintillator is surrounded by copper and lead shields, and plastic scintillators to reduce the background contribution from external radiation as well as tag and reject events associated with cosmic-ray muons [29]. Each NaI(Tl) crystal is optically coupled to two photomultiplier tubes (PMTs) with the signals recorded as $8 \mu\text{s}$ waveforms. A trigger is generated when a signal corresponding to one or more photoelectrons occurs in each PMT within a 200 ns time window [30].

The analysis presented here utilizes 1.7 years of data, previously used for the first annual modulation search [22], and background modeling with a 1 keVee energy threshold [31]. The data were acquired between October 21, 2016 and July 18, 2018. Three of the eight crystals were observed to have high noise rates in the region of interest (ROI) and were excluded from the analysis, resulting in an effective data exposure of 97.7 kg-year [21, 22].

It was found that PMT noise causes the majority of the triggered events in the ROI. A multivariable boosted decision tree (BDT) [32] was used to characterize the pulse-shapes to discriminate these PMT-induced noise events from radiation-induced scintillation events [21, 22]. To improve the discrimination power, a likelihood score was introduced as an input training variable to the BDT that rates how well the waveform matches either scintillation events or PMT-induced noise events. The likelihood score particularly enhances the removal of noise pulses and allows us to comfortably operate with a 1 keVee threshold [27]. The BDT is trained with samples

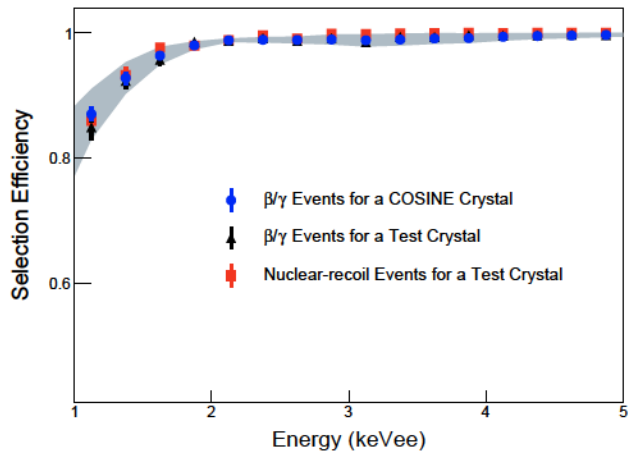


FIG. 1. Efficiencies for β/γ and nuclear-recoil events. Blue dots show the efficiencies for β/γ events for one of the COSINE-100 crystal. Black and red dots are efficiencies of β/γ and nuclear-recoil events, respectively, for a small-size test crystals. This test crystal was cut from the same ingot of the COSINE-100 crystal and used for the neutron beam measurement. All measurements are consistent within the systematic uncertainty of the efficiency shown in grey band.

of scintillation-rich ^{60}Co calibration data and PMT-noise dominant single-hit physics data. The multiple-hit events consist of in-time hits in multiple crystals or liquid scintillator that cannot be caused by dark matter interactions. The event selection efficiencies for scintillation events are evaluated with the ^{60}Co calibration dataset and cross-checked with the physics data, as well as nuclear recoil events. The efficiencies from the ^{60}Co calibration data were found to be consistent with previously measured efficiencies for nuclear recoil events obtained using a monoenergetic 2.42 MeV neutron beam [33] as shown in Fig. 1. The efficiency differences and their uncertainties are included as a systematic uncertainty.

Background modeling

Events in the remaining dark matter search dataset predominantly originate from environmental γ and β radiations. Sources include radioactive contaminants internal to the crystals or on their surfaces, external detector components, and cosmogenic activation [31]. In order to understand these events, the background spectrum for each individual crystal is modeled using computer simulations based on the Geant4 toolkit [34].

Events are classified according to their energy: 1–70 keVee are low energy and 70–3000 keVee are high energy. The single-hit and multiple-hit data are separated in the background modeling of the NaI(Tl) crystals. To understand the background spectra, Geant4-based simulation events are generated and recorded in a format that matches that of the COSINE-100 data acquisition

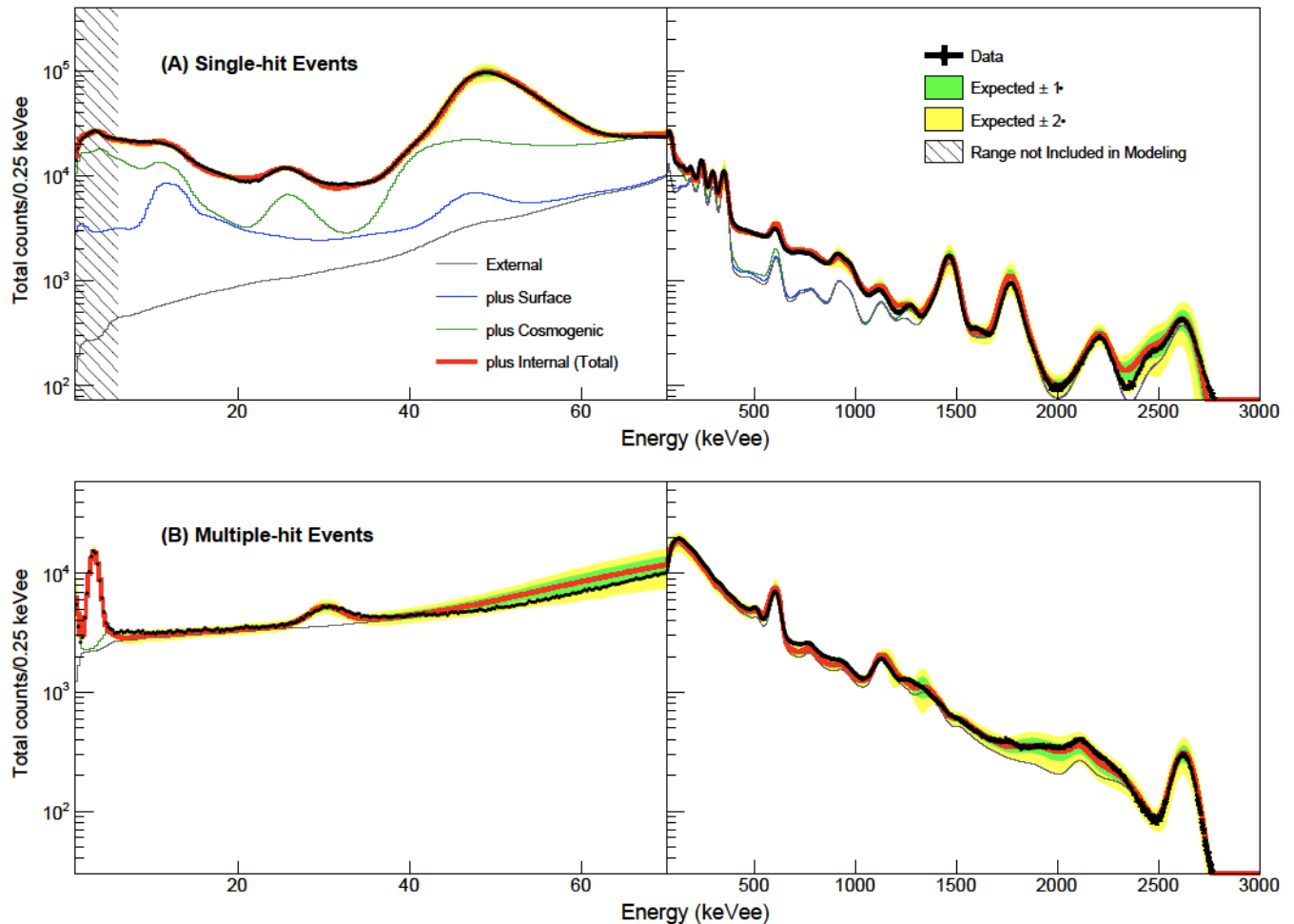


FIG. 2. Energy spectra of single-hit and multiple-hit events. Presented here are summed energy spectra for the five crystals (black dots) and their background models (red solid line) with the 68% and 95% confidence intervals. The expected contributions to the background from internal radionuclide contaminations, the surface of the crystals and nearby materials, cosmogenic activation, and external backgrounds are indicated. The 1–6 keV region of the single-hit spectrum is masked because these events are not used for the background modeling.

system. Energy resolutions and selection efficiencies for each crystal are applied. The fraction of each background component is determined from a simultaneous fit to the four measured distributions. For the single-hit events, only 6–3000 keVee events are used to avoid a bias of the WIMP signal in the ROI. Details of the background modeling for the dataset are described elsewhere [31].

The background components are divided into four categories: internal contamination, surface contamination, external sources and cosmogenic activation. The ^{238}U , ^{232}Th , ^{40}K , and ^{210}Pb contaminations in the crystal constitute the internal background. The ^{210}Pb contaminations on the crystal surface and adjacent materials are the surface component. Backgrounds from ^{238}U , ^{232}Th and ^{40}K in the PMTs, liquid scintillator, and the shield materials constitute the external sources. In order to estimate contributions from cosmogenic activation, we use

a time-dependent analysis that takes into account the cosmic-ray exposure time on the ground and the cooling time in the underground laboratory of each individual crystal [35].

The most dominant background components in the ROI are generated by internal radionuclide contamination and by cosmogenic activation. This includes ^{210}Pb and ^{40}K internal contaminants, and ^{210}Pb surface contamination. The contribution to the ROI from cosmogenic activation is mostly due to ^3H with some additional contributions from ^{113}Sn and ^{109}Cd . Background modeling was performed independently for each individual crystal, and Fig. 2 shows the accumulated result of the model fit to data and the systematic uncertainties.

Several sources of systematic uncertainty are identified and included in this analysis. The largest systematic uncertainties are those associated with the efficiencies,

which include statistical errors in the efficiency determinations with the ^{60}Co calibration and systematic errors derived from the independent cross-checks of the physics data and the nuclear recoil events. Uncertainties in the energy resolution and nonlinear responses of the NaI(Tl) crystals [36] affect the shapes of the background and signal spectra. The depth-profiles of ^{210}Pb on the surface of the NaI(Tl) crystals, studied with a ^{222}Rn contaminated crystal, are varied within their uncertainty [37]. Variations in the levels and the positions of external Uranium and Thorium decay-chain contaminants are also taken into account. Effects of event rate variations and possible distortions in the shapes of spectra are considered in systematic uncertainties.

Dark matter interpretations

We consider various WIMP models to determine the possible contribution from WIMP interactions to the measured energy spectra using the simulated data. The DAMA/LIBRA-phase2 data [9] were found not to be compatible with the canonical model [11, 26], which is an isospin-conserving spin-independent interaction between WIMP and nucleus in the specific context of the standard WIMP galactic halo model, and is the most commonly used interpretation of the direct detection of the WIMP dark matter [38]. However, an isospin-violating interaction in which the WIMP-proton coupling is different from the WIMP-neutron coupling, provides a good fit to the observed annual modulation signals from the DAMA/LIBRA-phase2 data [11, 26]. To interpret the DAMA/LIBRA data and compare with the COSINE-100 data, we use the best fit values of the effective coupling of WIMPs to neutrons and to protons (f_n/f_p) obtained for the simultaneous fit of DAMA/LIBRA-phase1 and DAMA/LIBRA-phase2 data described elsewhere [26]. We also interpret the results of the COSINE-100 data in the canonical model for the comparison with the DAMA/LIBRA-phase1 only data.

We use the nuclear recoil quenching factor (QF) from recent measurements with monoenergetic neutron beams [33] (quenching factor is the ratio of the scintillation light yield from sodium or iodine recoil relative to that for electron recoil for the same energy). In those measurements, neutron tagging detectors at a fixed angle relative to the incoming neutron beam direction provide unambiguous knowledge of the deposited energy. We obtained a strong energy dependence of the nuclear recoil QFs. Modelings of the QF measurements described in Ref. [26] are appropriated for this analysis (subsequently referred to as new QF). However, most studies interpreting the DAMA/LIBRA's results have used significantly larger QF values that were reported by the DAMA group in 1996 [39] (subsequently referred to as DAMA QF), that were obtained by measuring the response of NaI(Tl) crystals to nuclear recoils induced by neutrons from a ^{252}Cf source. The best description of the

measured nuclear recoil spectra from the ^{252}Cf source obtained $30\pm 1\%$ and $9\pm 1\%$ for the sodium and iodine QF values, respectively, assuming no energy dependence of the QF values. The values obtained from the new measurements are approximately 13% and 5% for the sodium and iodine, respectively, at 20 keVnr where keVnr is kilo-electron volt nuclear recoil energy [26]. Efficient noise rejection as well as correct evaluation of trigger and selection efficiencies are essential for proper estimation of the quenching factors [33, 40, 41]. Even though the measurements of the DAMA QF values were required to check the efficiency evaluations as well as no energy-dependent QF assumption [40], the hypothesis of different QFs [25] in the NaI(Tl) crystals used by DAMA/LIBRA and COSINE-100 needs to be checked. Note that results from the analysis of the previous 59.5 days of COSINE-100 data with a 2 keVee threshold were not sufficient to exclude all the DAMA/LIBRA 3σ regions when different QFs are used [26].

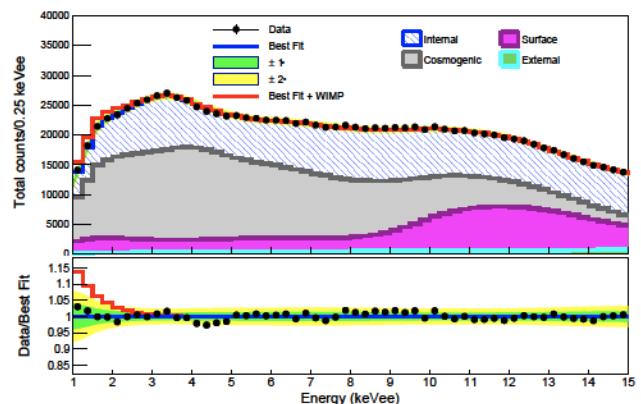


FIG. 3. Example fit results for a $11.5 \text{ GeV}/c^2$ WIMP mass in the case of $f_n/f_p = -0.76$. Presented here is the summed energy spectrum for the five crystals (black filled circles shown with 68% confidence level error bars) and the best fit (blue line) for which no WIMP signals are obtained. Fitted contributions to the background from internal radionuclide contaminations, the surface of the crystals and nearby materials, cosmogenic activation, and external backgrounds are indicated. The green (yellow) bands are the 68% (95%) confidence level intervals of the systematic uncertainty obtained from the likelihood fit. For presentation purposes, we indicate the signal shape (red line) assuming a WIMP-proton cross section of $2.5 \times 10^{-2} \text{ pb}$ corresponding to the DAMA best fit value for the WIMP-sodium interaction using the DAMA QF values.

To search for evidence of a WIMP signal in the data, a Bayesian approach with a likelihood function based on Poisson probability is used. The likelihood fit is applied to the measured single-hit energy spectra between 1 and 15 keVee for each WIMP model for several masses. Each crystal is fitted with a crystal-specific background model and a crystal-correlated WIMP signal for the combined fit by multiplying the five crystals' likelihoods. Means

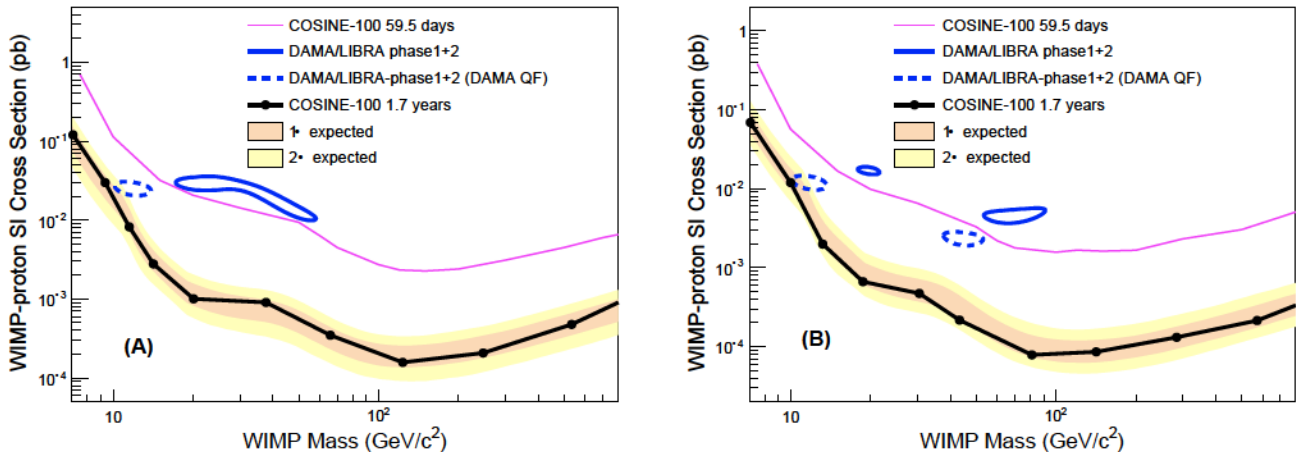


FIG. 4. Exclusion limits on the WIMP-proton spin-independent cross section for the isospin-violating interaction. The 3σ allowed regions of the WIMP mass and the WIMP-proton cross-section associated with the DAMA/LIBRA-phase1+phase2 data (blue solid contours) using the new QF values in their best fit for (A) sodium scattering and (B) iodine scattering hypotheses are compared with the 90% confidence level exclusion limits from the COSINE-100 data (black-solid-line), together with the 68% and 95% probability bands for the expected 90% confidence level limit assuming the background-only hypothesis. The dashed blue contours show the allowed regions of the DAMA/LIBRA-phase1+phase2 data using the DAMA QF values. For comparison, limits from the initial 59.5 days COSINE-100 data [21] are shown by the purple-solid-line. In each plot, we fix the effective coupling ratios to neutrons and protons f_n/f_p to the best fit values of the DAMA data.

and uncertainties for background components, which are determined from the modeling [31], are used to set Gaussian priors for the background. The systematic uncertainties are included in the fit as nuisance parameters with Gaussian priors (see the section of materials and methods).

A good fit to the DAMA/LIBRA-phase2 data was obtained with the isospin-violating interaction [11, 26]. We simultaneously use the DAMA/LIBRA-phase1 and phase2 data to fit three parameters: the WIMP mass, the WIMP-proton cross-section, and f_n/f_p . The best fits were obtained for two different values of f_n/f_p favoring WIMP-sodium and WIMP-iodine interactions as $f_n/f_p = -0.76$ and -0.71 , respectively. For the best fit values of f_n/f_p , the 3σ allowed regions in the WIMP-mass and the WIMP-proton cross-section parameter spaces are obtained [26].

The COSINE-100 data are fitted to each of the different WIMP masses for each f_n/f_p value using only the new QF values. An example of a maximum likelihood fit for a $11.5 \text{ GeV}/c^2$ WIMP and $f_n/f_p = -0.76$ WIMP signal is presented in Fig. 3. The summed event spectrum for the five crystals is shown together with the best-fit result. For comparison, the expected signal for a $11.5 \text{ GeV}/c^2$ WIMP with a spin-independent WIMP-proton cross section of $2.5 \times 10^{-2} \text{ pb}$, the central value of the DAMA/LIBRA best fit using the DAMA QF values for the WIMP-sodium interaction, is shown by the red solid line. No excess of events that could be attributed to WIMP interactions is found for the considered WIMP signals. The posterior probabilities of signals are con-

sistent with zero in all cases and 90% confidence level limits are determined (see Fig. S10). Figure 4 shows the 3σ contours of the DAMA/LIBRA data in the best fit values of f_n/f_p using the new QF values and the DAMA QF values together with the 90% confidence level upper limits from the COSINE-100 data using the same f_n/f_p and the new QF values. The 90% confidence level limits from the 1.7 years COSINE-100 data show approximately an order of magnitude better limits than those of our previous results using 59.5 days data and exclude the DAMA/LIBRA allowed 3σ regions for both sets of QF values.

Even though the DAMA/LIBRA-phase2 data do not fit well to the canonical model, their phase1 data has been shown to be well fit with an isospin-conserving spin-independent WIMP-nuclei interaction [10, 26]. The 90% confidence level upper limits from the COSINE-100 data for the canonical model are also obtained. Figure 5 shows the 3σ allowed regions that are associated with the DAMA/LIBRA-phase1 signal using the new QF values and the DAMA QF values together with the 90% confidence level upper limits from the COSINE-100 data using the new QF values. These limits mostly exclude the DAMA/LIBRA allowed region even when different QF values are considered for each experiment.

In addition, we have checked each operator in an assortment of non-relativistic effective field theory models where previous null results from the 59.5 days COSINE-100 data do not fully cover the 3σ regions of the DAMA/LIBRA data for a few operators [23]. The 1.7 years data is now found to fully cover the 3σ allowed

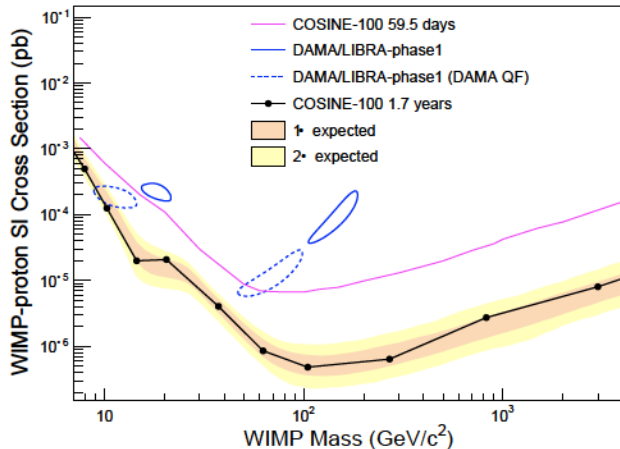


FIG. 5. Exclusion limits on the WIMP-nucleon spin-independent cross section of the isospin-conserving interaction. The observed (filled circles with black solid line) 90% confidence level exclusion limits on the WIMP-nucleon spin-independent cross section from the COSINE-100 are shown together with the 68% and 95% probability bands for the expected 90% confidence level limit, assuming the background-only hypothesis. The limits are compared with a WIMP interpretation of the DAMA/LIBRA-phase1 3σ allowed region using the new QF (blue-solid-contours) and the DAMA QF (blue-dashed-contours) [10].

regions for each model assuming the DAMA QF values, as can be seen in Fig. 6.

DISCUSSION

After the release of the initial 59.5 days COSINE-100 data with null observations using the same NaI(Tl) target material, a few possibilities were suggested that preserve the consistency between the DAMA/LIBRA and COSINE-100 results [23, 25, 26]. The results of this analysis, with 1.7 years accumulated COSINE-100 data and improved analysis technique with a 1 keVee energy threshold do not favor these suggested possibilities. A model independent data analysis of the annual modulation with several years COSINE-100 data is required for an unambiguous conclusion, nevertheless the results presented here provide strong constraints on the dark matter interpretation of the DAMA/LIBRA annual modulation signals with the same NaI(Tl) target materials.

ACKNOWLEDGMENTS

We thank the Korea Hydro and Nuclear Power (KHNP) Company for providing underground laboratory space at Yangyang. This work is supported by: the Institute for Basic Science (IBS) under project

code IBS-R016-A1 and NRF-2021R1A2C3010989, Republic of Korea; NSF Grants No. PHY-1913742, DGE-1122492, WIPAC, the Wisconsin Alumni Research Foundation, United States; STFC Grant ST/N000277/1 and ST/K001337/1, United Kingdom; Grant No. 2017/02952-0 FAPESP, CAPES Finance Code 001, CNPq 131152/2020-3, Brazil.

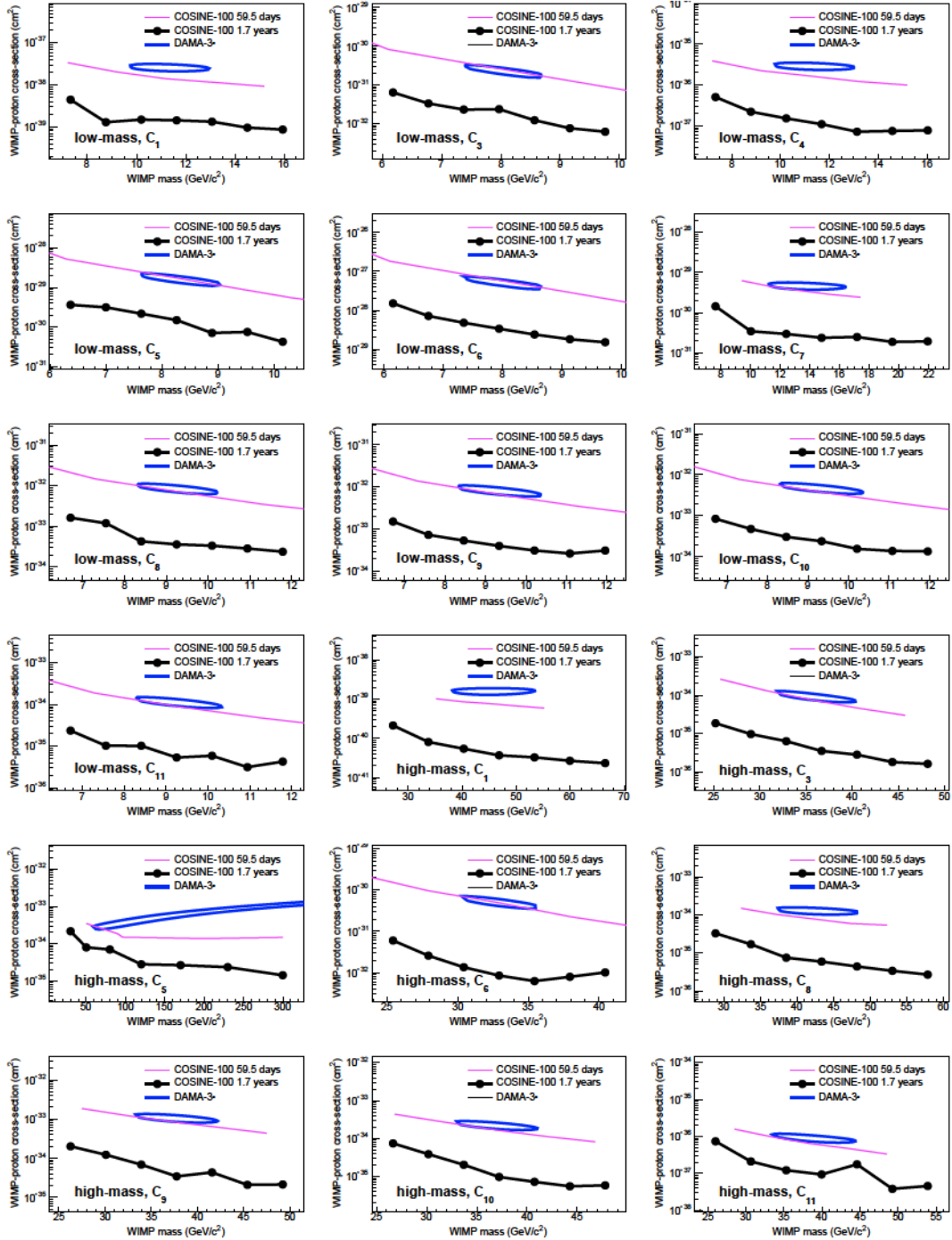


FIG. 6. Exclusion limits on the WIMP-proton cross section for the effective field theory operators. DAMA/LIBRA 3σ allowed regions (blue contours) and COSINE-100 90% confidence level exclusion limits of previous analysis (pink solid lines) and this work (black dots and lines) on the WIMP-proton cross sections for a variety of effective field theory operators using the DAMA QF values are presented. For each operator, f_n/f_p is fixed to the corresponding best fit value of the DAMA/LIBRA data.

\mathcal{L}

—

\mathcal{L}

\mathcal{L}

$$\frac{\mathcal{L}}{\mathcal{L}} \quad \frac{\mathcal{L}}{\mathcal{L}}$$

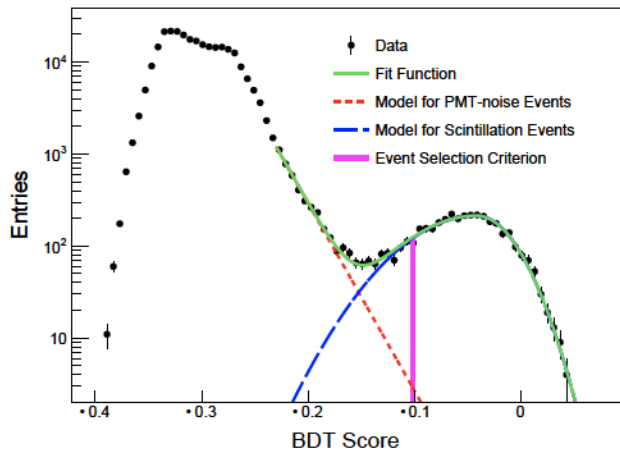


FIG. 7. BDT-score distribution of events at the 1–1.25 keV. The BDT distribution of the single-hit physics data is fitted by the green function that consists of an asymmetric Gaussian distribution for the scintillation events (dashed blue) and an exponential function for the PMT-noise events (dotted red). The thick magenta line shows a BDT criterion for the event selection.

data and the single-hit physics data.

systematic uncertainties

In addition to the statistical uncertainties in the background and signal models, various sources of systematic uncertainties are taken into account. Errors in the selection efficiency, the energy resolution, the energy scale, and background modeling technique translate into uncertainties in the shapes of the signal and background probability density functions, as well as to rate changes. These quantities are allowed to vary within their uncertainties as nuisance parameters in the likelihood fit.

The most influential systematic uncertainty is the error associated with the efficiencies shown as the shaded region in Fig. 1. This is because the efficiency systematic uncertainty maximally covers the statistical uncertainties in the ROI. We include two types of systematic variations in the efficiency error. At first, we account maximum variations of the uncertainty across the width of the energy bin to provide $\pm 1\sigma$ ranges as shown in Fig. 8 (A). Relative uncertainties shown in Fig. 8 (B) are included as nuisance parameters of the background and signal in the likelihood function (see Eq. 8 and Eq. 9). However, due to the dominant errors in the ROI, we consider maximum shape distortions that can mimic the WIMP signal as shown in Fig. 8 (C). Its relative uncertainty is shown in Fig. 8 (D) and included as a nuisance parameter.

In the background model fit, the levels of background activities are limited by Gaussian constraint terms added to the likelihood function as determined by measured activities and their uncertainties. The systematic uncer-

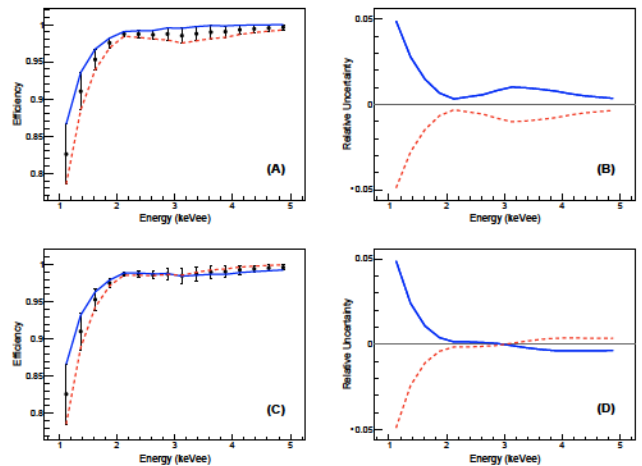


FIG. 8. Systematic uncertainty of the event selection efficiency. Black dots with error bars in (A) and (C) present the event selection efficiency and associated systematic uncertainty. (A) The upper (blue-solid line) and lower (red-dashed line) limits in 1σ uncertainties and (B) their associated relative uncertainty are shown. In addition, the maximum distortions of shape that can mimic the WIMP signal are accounted (C). Here the blue-solid line starts from the upper 1σ in the first energy bin (1–1.25 keV) and evenly moves to the lower -1σ in the last energy bin (4.75–5 keV). The red-dashed line represent the opposite changes of the efficiency systematic. (D) Relative uncertainties associated with (C) are shown. The efficiency systematic is accounted as nuisance parameters in the likelihood using above two-types of the relative uncertainties.

tainties associated with the background modeling include the uncertainties of the activities estimated by the background model fit. In addition, different locations of external radioactive contaminations are taken into account by generating external contributions at different positions. Background contributions from ^{210}Pb contamination on the surface of the NaI(Tl) crystals were studied with a small NaI(Tl) crystal exposed to ^{222}Rn from a ^{226}Ra source [37]. Depth profiles from two exponential components were modeled to fit the ^{222}Rn contaminated crystal and matched to the test-setup data [31]. Uncertainties in the measured depth profiles are propagated into systematic uncertainties. We generate the background model associated with each systematic variation and account relative uncertainty to be added as the nuisance parameter.

The energy calibration is performed by tracking the positions of internal β and γ peaks from radioactive contaminations in the crystals, as well as with external γ sources [31]. The nonlinear detector response of the NaI(Tl) crystals [36] in the low energy region is modeled with an empirical function across all crystals [31]. Subtle differences for each crystal from the general non-linearity model of the NaI(Tl) crystals are evaluated to consider the systematic uncertainty on the energy scale.

— —

—

— —

—

\mathcal{P}

\mathcal{L}

\mathcal{P}

\mathcal{L}

\mathcal{L}

—

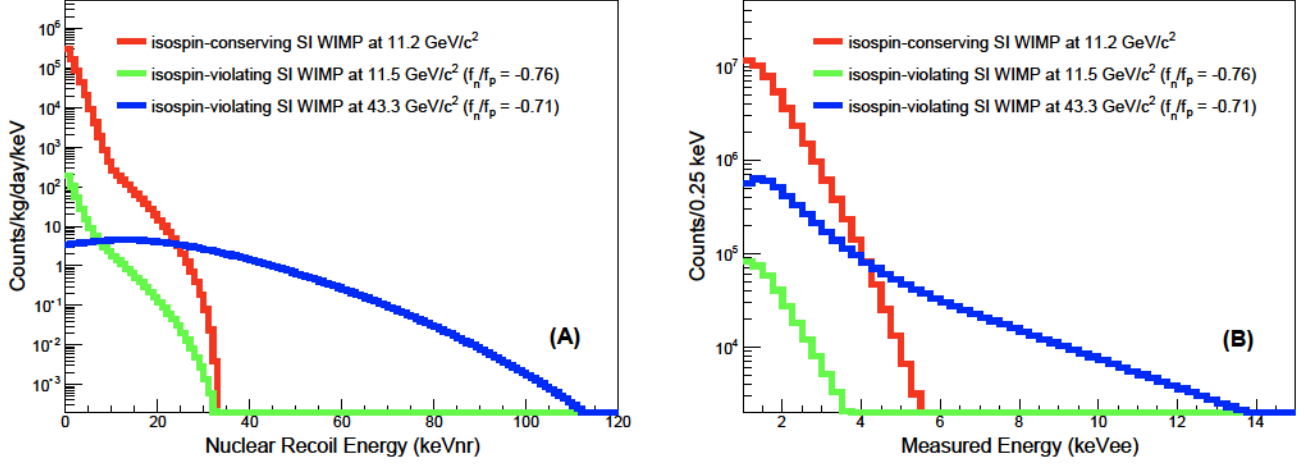


FIG. 9. Energy spectra of the WIMP signal. (A) Raw energy spectra for three different WIMP models with WIMP-proton cross section of 1 pb. (B) The expected energy spectra with WIMP-proton cross section of 1 pb for the three WIMP models when taking account of the quenching factors, detector resolutions, and selection efficiencies assuming 1.7 years COSINE-100 data.

of events in the signal and background,

$$E_{ij}(\sigma_{\text{WIMP}}, \alpha, \beta) = S_{ij}(\sigma_{\text{WIMP}}, \alpha) + B_{ij}(\alpha, \beta), \quad (7)$$

where the number of background events $B_{ij}(\alpha, \beta)$ and signal events $S_{ij}(\sigma, \alpha)$ are generated from the simulated experiments through the background modeling and the WIMP signal discussed above, with effects by systematic uncertainties. The systematic uncertainty affecting the background model is included as a function of the nuisance parameter α and β , as

$$B_{ij}(\alpha, \beta) = \prod_k^{N_{\text{sys}}} (1 + \alpha_{ik} \epsilon_{ijk}) \prod_l^{N_{\text{bkgd}}} (1 + \beta_{il}) \cdot B_{ij}^{\text{MC}}, \quad (8)$$

where B_{ij}^{MC} is the number of background events obtained from the model. The nuisance parameter α_{ik} controls the effect of the energy-dependent uncertainty, ϵ_{ijk} , which is 1σ relative error for k^{th} systematic uncertainty. Meanwhile, another nuisance parameter β_{il} adjusts the activity for l^{th} background component. The corresponding impact on the WIMP signal is considered by means of the expression,

$$S_{ij}(\sigma_{\text{WIMP}}, \alpha) = \prod_k^{N_{\text{sys}}} (1 + \alpha_{ik} \epsilon_{ijk}) \cdot T_i \cdot M_i \cdot R_j(\sigma_{\text{WIMP}}; m_\chi), \quad (9)$$

where M_i and T_i denote the mass and data exposure for crystal i , and R_j is the expected rate of WIMP-proton

interaction through an integration of dR/dE_{ee} in the j^{th} energy bin. Each nuisance parameter is constrained with evaluated uncertainty assuming a Gaussian distribution,

$$\pi(\alpha, \beta) = \prod_i^{N_{\text{crystal}}} \prod_k^{N_{\text{sys}}} \exp\left[-\frac{\alpha_{ik}^2}{2}\right] \prod_l^{N_{\text{bkgd}}} \exp\left[-\frac{\beta_{il}^2}{2\delta_{il}^2}\right], \quad (10)$$

where δ_{il} is the uncertainty of the activity of the l^{th} background component. A Markov Chain Monte Carlo [50, 51] via Metropolis-Hastings algorithm [52, 53] is used for the multivariable integration in posterior PDF. We developed our own Bayesian tool for this process. A comparison with a publicly available Bayesian analysis toolkit [54] was done for the initial 59.5 days COSINE-100 data and both tools showed consistent results.

To avoid biasing the WIMP search, the fitter was tested with simulated event samples. Each experimental data is prepared by Poisson random extraction from the modeled background spectrum [31], assuming a background-only hypothesis. Marginalization to obtain the posterior PDF for each simulation sample is performed to set the 90% confidence level exclusion limits as shown in Fig. 10. The 1000 simulated experiments result in 68% and 95% bands of the expected limit presented in Figs. 4 and 5. The data fits are done in the same way as the simulated data. Figure 10 shows the posterior PDFs and their cumulative distribution functions (CDFs) of data for two different WIMP models. The CDF provides the 90% confidence level exclusion limit for each fit.

[1] D. Clowe et al., A direct empirical proof of the existence of dark matter, *Astrophys. J.* **648**, L109

(2006).

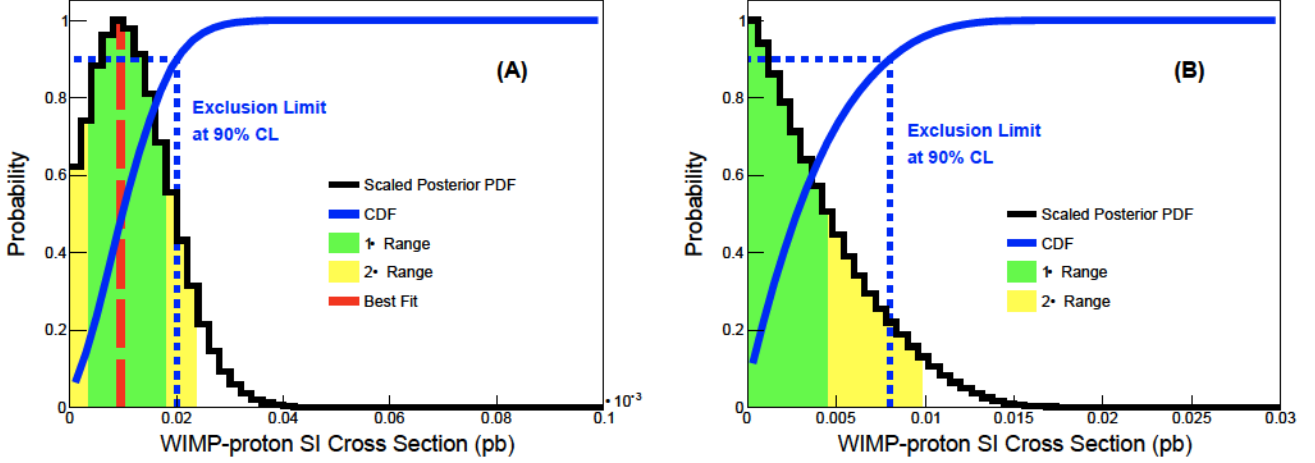


FIG. 10. Posterior probability density functions. Two examples of the posterior PDFs and their CDFs for the 1.7 years COSINE-100 data for different WIMP models. (A) is the canonical model for a WIMP mass of $20.4 \text{ GeV}/c^2$ and (B) is the isospin-violating case with WIMP mass $11.5 \text{ GeV}/c^2$ and $f_n/f_p = -0.76$. The posterior PDFs are scaled for the maximum to be unity. The exclusion limit at 90% confidence level is obtained from CDF matched with 0.9. Green and yellow areas represent the 68% and 95% of confidence intervals, respectively. In the case of (A), the best fit value (red-dashed line) presents slightly positive result of WIMP-proton cross section $9.5 \times 10^{-5} \text{ pb}$, but within 95% region. We, therefore, set the 90% confidence level upper limit.

- [2] P. A. R. Ade et al., (Planck Collaboration), Planck 2015 results. XIII. Cosmological parameters, *Astron. Astrophys.* **594**, A13 (2016).
- [3] H. Baer, K.-Y. Choi, J. E. Kim, and L. Roszkowski, Dark matter production in the early Universe: beyond the thermal WIMP paradigm, *Phys. Rept.* **555**, 1–60 (2015).
- [4] B. W. Lee and S. Weinberg, Cosmological lower bound on heavy-neutrino masses, *Phys. Rev. Lett.* **39**, 165 (1977).
- [5] M. W. Goodman and E. Witten, Detectability of Certain Dark Matter Candidates, *Phys. Rev. D* **31**, 3059 (1985).
- [6] M. Battaglieri et al., US Cosmic Visions: New Ideas in Dark Matter 2017: Community Report, in *U.S. Cosmic Visions: New Ideas in Dark Matter College Park, MD, USA, March 23–25, 2017*. arXiv:1707.04591.
- [7] R. Bernabei et al., (DAMA Collaboration Collaboration), Searching for wimps by the annual modulation signature, *Phys. Lett. B* **424**, 195–201 (1998).
- [8] R. Bernabei et al., (DAMA/LIBRA Collaboration), Final model independent result of DAMA/LIBRA-phase1, *Eur. Phys. J. C* **73**, 2648 (2013).
- [9] R. Bernabei et al., (DAMA/LIBRA Collaboration), First Model Independent Results from DAMA/LIBRA-Phase2, *Nucl. Phys. At. Energy* **19**, 307 (2018).
- [10] C. Savage, G. Gelmini, P. Gondolo, and K. Freese, Compatibility of DAMA/LIBRA dark matter detection with other searches, *JCAP* **0904**, 010 (2009).
- [11] S. Baum, K. Freese, and C. Kelso, Dark Matter implications of DAMA/LIBRA-phase2 results, *Phys. Lett. B* **789**, 262–269 (2019).
- [12] S. Kang, S. Scopel, G. Tomar, and J.-H. Yoon, DAMA/LIBRA-phase2 in WIMP effective models, *JCAP* **1807**, 016 (2018).
- [13] E. Aprile et al., (XENON Collaboration), Search for Electronic Recoil Event Rate Modulation with 4 Years of XENON100 Data, *Phys. Rev. Lett.* **118**, 101101 (2017).
- [14] E. Aprile et al., (XENON Collaboration), Dark Matter Search Results from a One Tonne \times Year Exposure of XENON1T, *Phys. Rev. Lett.* **121**, 111302 (2018).
- [15] D. S. Akerib et al., (LUX Collaboration), Search for annual and diurnal rate modulations in the LUX experiment, *Phys. Rev. D* **98**, 062005 (2018).
- [16] K. W. Kim et al., Tests on NaI(Tl) crystals for WIMP search at the Yangyang Underground Laboratory, *Astropart. Phys.* **62**, 249 (2015).
- [17] G. Adhikari et al., (COSINE-100 Collaboration), Initial Performance of the COSINE-100 Experiment, *Eur. Phys. J. C* **78**, 107 (2018).
- [18] B. Suerfu, M. Wada, W. Peloso, M. Souza, F. Calaprice, J. Tower, and G. Ciampi, Growth of Ultra-high Purity NaI(Tl) Crystal for Dark Matter Searches, *Phys. Rev. Research* **2**, 013223 (2020).
- [19] K. Fushimi et al., Development of highly radiopure NaI(Tl) scintillator for PICOLON dark matter search project, *PTEP* **2021**, 043F01 (2021).
- [20] J. Amare et al., Annual Modulation Results from Three Years Exposure of ANAIS-112, *Phys. Rev. D* **103**, 102005 (2021).
- [21] G. Adhikari et al., (COSINE-100 Collaboration), An experiment to search for dark-matter interactions using sodium iodide detectors, *Nature* **564**, 83 (2018).
- [22] G. Adhikari et al., (COSINE-100 Collaboration), Search for a dark matter-induced annual modulation signal in NaI(Tl) with the COSINE-100 experiment,

- Phys. Rev. Lett.* , 031302 (2019).
- [23] G. Adhikari et al., (COSINE-100 and Sogang Phenomenology Group Collaboration), COSINE-100 and DAMA/LIBRA-phase2 in WIMP effective models, *JCAP* , 048 (2019).
- [24] A. Zhitnitsky, DAMA/LIBRA annual modulation and Axion Quark Nugget Dark Matter Model, *Phys. Rev. D* , 083020 (2020).
- [25] R. Bernabei et al., The DAMA project: Achievements, implications and perspectives, *Prog. Part. Nucl. Phys.* , 103810 (2020).
- [26] Y. J. Ko et al., (COSINE-100 Collaboration), Comparison between DAMA/LIBRA and COSINE-100 in the light of Quenching Factors, *JCAP* , 008 (2019).
- [27] G. Adhikari et al., (COSINE-100 Collaboration), Lowering the energy threshold in COSINE-100 dark matter searches, *Astropart. Phys.* , 102581 (2021).
- [28] G. Adhikari et al., The COSINE-100 liquid scintillator veto system, *Nucl. Instrum. Meth. A* , 165431 (2021).
- [29] H. Prihtiadi et al., (COSINE-100 Collaboration), Muon detector for the COSINE-100 experiment, *JINST* , T02007 (2018).
- [30] G. Adhikari et al., (COSINE-100 Collaboration), The COSINE-100 Data Acquisition System, *JINST* , P09006 (2018).
- [31] G. Adhikari et al., (COSINE-100 Collaboration), Background modeling for dark matter search with 1.7 years of cosine-100 data, [arXiv:2101.11377](https://arxiv.org/abs/2101.11377).
- [32] J. H. Friedman, Greedy function approximation: A gradient boosting machine, *Ann. Stat.* , 1189 (2001).
- [33] H. W. Joo, H. S. Park, J. H. Kim, S. K. Kim, Y. D. Kim, H. S. Lee, and S. H. Kim, Quenching factor measurement for NaI(Tl) scintillation crystal, *Astropart. Phys.* , (2019).
- [34] S. Agostinelli et al., (GEANT4 Collaboration), GEANT4: A Simulation toolkit, *Nucl. Instrum. Meth. A* , 250 (2003).
- [35] E. Barbosa de Souza et al., (COSINE-100 Collaboration), Study of cosmogenic radionuclides in the COSINE-100 NaI(Tl) detectors, *Astropart. Phys.* , 102390 (2020).
- [36] L. Swiderski, Response of doped alkali iodides measured with gamma-ray absorption and Compton electrons, *Nucl. Instrum. Meth. A* , 42 (2013).
- [37] G. H. Yu, C. Ha, E. J. Jeon, K. W. Kim, N. Y. Kim, Y. D. Kim, H. S. Lee, H. K. Park, and C. Rott, Depth profile study of ^{210}Pb in the surface of an NaI(Tl) crystal, *Astropart. Phys.* , 102518 (2021).
- [38] M. Tanabashi et al., (Particle Data Group Collaboration), Review of Particle Physics, *Phys. Rev. D* , 030001 (2018).
- [39] R. Bernabei et al., (DAMA Collaboration), New limits on WIMP search with large-mass low-radioactivity NaI(Tl) set-up at Gran Sasso, *Phys. Lett. B* , 757 – 766 (1996).
- [40] J. I. Collar, Quenching and channeling of nuclear recoils in NaI(Tl): Implications for dark-matter searches, *Phys. Rev. C* , 035806 (2013).
- [41] J. Xu et al., Scintillation Efficiency Measurement of Na Recoils in NaI(Tl) Below the DAMA/LIBRA Energy Threshold, *Phys. Rev. C* , 015807 (2015).
- [42] H. Prihtiadi et al., (COSINE-100 Collaboration), Measurement of the cosmic muon annual and diurnal flux variation with the COSINE-100 detector, *JCAP* , 013 (2021).
- [43] K. Freese, J. A. Frieman, and A. Gould, Signal Modulation in Cold Dark Matter Detection, *Phys. Rev. D* , 3388–3405 (1988).
- [44] M. C. Smith et al., The RAVE survey: constraining the local Galactic escape speed, *Monthly Notices of the Royal Astronomical Society* , 755–772 (2007).
- [45] V. Gluscevic, M. I. Gresham, S. D. McDermott, A. H. G. Peter, and K. M. Zurek, Identifying the Theory of Dark Matter with Direct Detection, *JCAP* , 057 (2015).
- [46] N. Anand, A. L. Fitzpatrick, and W. C. Haxton, Weakly interacting massive particle-nucleus elastic scattering response, *Phys. Rev. C* , 065501 (2014).
- [47] A. L. Fitzpatrick, W. Haxton, E. Katz, N. Lubbers, and Y. Xu, The Effective Field Theory of Dark Matter Direct Detection, *JCAP* , 004 (2013).
- [48] M. I. Gresham and K. M. Zurek, Effect of nuclear response functions in dark matter direct detection, *Phys. Rev. D* , 123521 (2014).
- [49] V. Gluscevic and S. D. McDermott, dmdd: Dark matter direct detection, Astrophysics Source Code Library [ascl:1506.002], 2015.
- [50] W. Gilks, S. Richardson, and D. Spiegelhalter, *Markov Chain Monte Carlo in Practice*. Boca Raton: Chapman & hall/CRC, 2006.
- [51] D. Gamerman and H. F. Lopes, *Markov Chain Monte Carlo*. Boca Raton: Chapman & hall/CRC, 2006.
- [52] N. Metropolis, A. W. Rosenbluth, M. N. Rosenbluth, and A. H. Teller, Equation of State Calculations by Fast Computing Machines, *J. Chem. Phys.* , 1087 (1953).
- [53] W. K. Hastings, Monte carlo sampling methods using markov chains and their applications, *Biometrika* , 97–109 (1970).
- [54] A. Caldwell, D. Kollár, and K. Kroninger, BAT: The Bayesian Analysis Toolkit, *Comput. Phys. Commun.* , 2197 (2009).